



Electrochemical stability and capacitance of in-situ synthesized Prussian blue on thermally-activated graphite

O. Charles Nwamba¹ · Elena Echeverria² · David N. McIlroy² · Jean'ne M. Shreeve¹ · D. Eric Aston³

© Springer Nature Switzerland AG 2019

Abstract

The search has been on for years to find at least, a stable, high surface area scaffold for Prussian blue (PB) and its analogs. If successful, PB's vast potential applications could be practicable. This, is besides other innate issues with PB such as poor cycle stability, low electronic conductivity to mention a few. For the first time, a stable Prussian blue@thermally activated graphite felt scaffold, with cycling stability of 2100 cycles, from -0.5 to 1.3 V, and in 1 M KCl, for at least 36 h is reported. At the end of 2100 CV cycles, sample capacitance more than tripled (381 mF cm^{-2} compared to 120 mF cm^{-2} at start of experiment). These properties suggest a practical ion-sieve for specific cation removal from contaminated water. Two new synthesis protocols were employed to achieve this: (a) a first time, single solution PB synthesis without externally applied potential, current or even elevated temperature and (b) a two-step solution-dipping process not involving acidic conditions. PB from both protocols exhibited similar electrochemical characteristics even though the electron relay paths along their charge transfer complexes are different. When probed for its HOMO characteristics, the PB@thermally-treated graphite showed no significant electronic difference from the thermally-treated felt scaffold, suggesting non-compromise of the treated graphite by the PB. Besides cation removal, the electrochemical and electronic properties of these PB@treated graphites suggest multiple electrochemical, non-electrochemical and electronic applications with intact structural and functional integrity.

Electronic supplementary material The online version of this article (<https://doi.org/10.1007/s42452-019-0713-z>) contains supplementary material, which is available to authorized users.

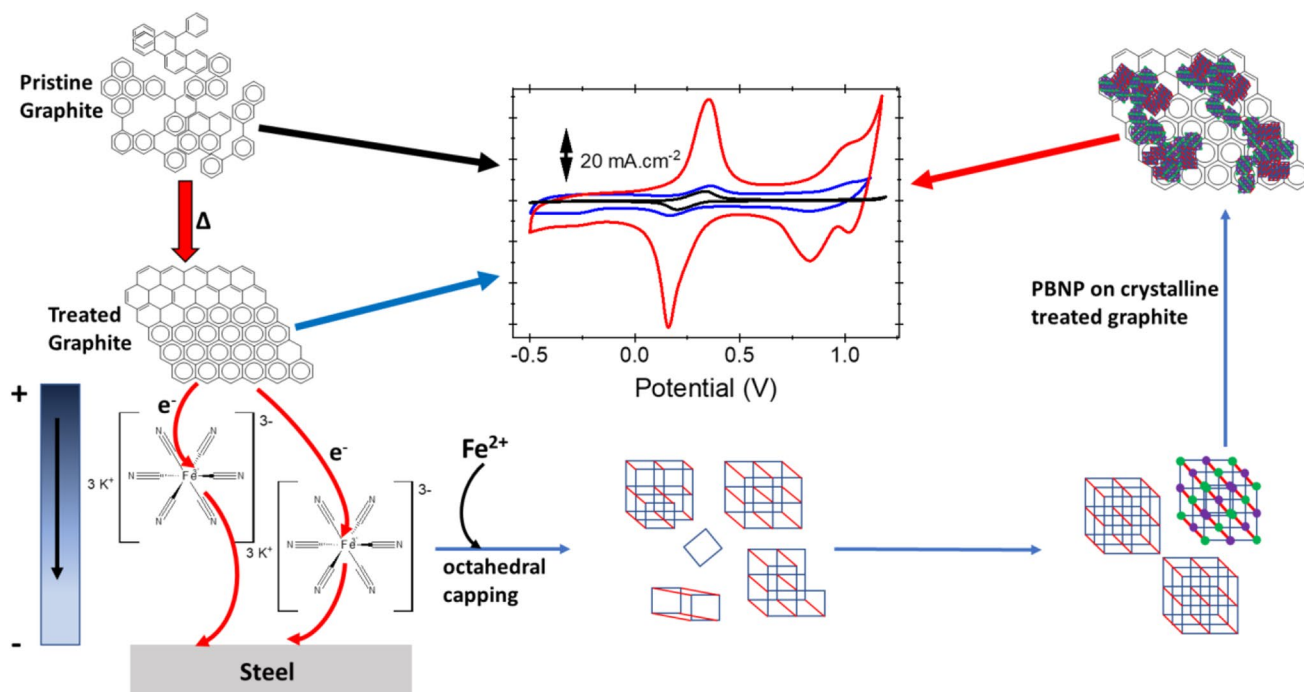
✉ D. Eric Aston, aston@uidaho.edu | ¹Department of Chemistry, University of Idaho, 875 Perimeter Drive MS 2343, Moscow, ID 83844-2343, USA. ²Department of Physics, Oklahoma State University, 145 Physical Science Bldg., Stillwater, OK 74078, USA. ³Department of Chemical and Materials Engineering, University of Idaho, 875 Perimeter Drive MS 1021, Moscow, ID 83844-1021, USA.



SN Applied Sciences (2019) 1:731 | <https://doi.org/10.1007/s42452-019-0713-z>

Received: 18 January 2019 / Accepted: 4 June 2019 / Published online: 17 June 2019

Graphic abstract Thermal activation of graphite felt increases capacitance while Prussian blue formation, either by metal-aided catalysis or the solution-dip method, further increases capacitance for the composite matrix.



Keywords Prussian blue · Graphite · Coordination polymers (CPs) · Thermal treatment · Capacitance · Charge relay path

1 Introduction

Metal coordination polymers (CPs), generated by the self-assembly of inorganic ligands and metal ions, are attractive materials for molecular capture, deliver/release, and sensing in aqueous media [1]. The design of these compounds is based on the formation of inorganic ligand coordination networks—polycyanometalate (PCM) anions—and “capping” metal cations. It also depends on hydrogen bonding between the PCMs and organic proton donors to transition from purely inorganic to metal–organic frameworks (MOFs). These transitions broaden the scope of MOF properties, allowing for their fine-tuning: a necessary requirement for the rational design of functional materials [2].

One such CPs, similar to MOFs, is Prussian blue (PB), a cyanide-bridged coordination compound between two Fe species in different oxidation states. PB is traditionally synthesized by mixing the metal ion, Fe³⁺ (Fe²⁺) and a corresponding metal octahedral complex, hexacyanoferrate (hexacyanoferrate) in an acidic solution [3]. It has the general formula $A_x\text{Fe}^{\text{III}}[\text{Fe}^{\text{II}}(\text{CN})_6]_y \cdot \varphi_{1-y} \cdot n\text{H}_2\text{O}$ ($n = 14\text{--}16$), where A is an alkali metal ion, K⁺ or Na⁺, (for the “soluble” PB which is often a dispersed yet lyophobic colloid) and φ

represents $[\text{Fe}(\text{CN})_6]^{4-}$ vacancies occupied by coordinating water ($0 < x < 1$; $0.75 < y < 1$) [4, 5]. The “capping” cation (Fe³⁺) in PB can be substituted for some other cation or polycation to tune the chemistry for application of the resultant PB analogue (PBA).

Due to their porosity and host–guest chemical features, PB, PBAs and their composites act as ion-sieve zeolites and membranes [6] to capture (and subsequently release) ions such as Cs⁺, Rb⁺ and Tl⁺ from radioactive waste-contaminated lands or environments [7–9] and even from the human body (i.e., detoxification) [1, 9–12]. PB is electrochromic [13], exhibiting three stable oxidation states at different potentials [4, 13–15]. It also exhibits electrochemical and magnetic properties [15], making PB and PBAs viable applicants in photoelectrochemical, photocatalytic, photomagnetic and magneto-optic devices [16]. Its electrochromic property is exploited in sensing [17, 18], photothermal therapy and optical imaging [19–21], photoacoustic imaging [12, 22], electrocatalysis [9, 16, 23], and theranostics—drug delivery/release agents in sites with poor drug accessibility, for example in cancer therapy [12, 24, 25]. PB, PBAs or their composites are further used as energy storage and conversion devices [9, 23] in batteries [4, 26–29], supercapacitors [30, 31], and fuel cells [28, 32].

Irrespective of the current and prospective applications of PB and PBAs for advanced functions, some serious shortcomings limit or even eliminate their utilization potentials. These failings include the large interstitial voids in PB, the localized valence electrons of the metals, which prohibit full electron delocalization, and the defects in the PB(A)s frameworks, thus resulting in low electronic conductivity [4, 33, 34]. The consequences are sluggish electron transfer kinetics from widening the cathodic and anodic peak potential differences, ΔE_p [34], and poor cycling stability [1, 35, 36]. Thus, proposed applications that depend, for example, on the above-mentioned properties would be severely impeded, such as in catalysis, electrochromic applications and, by inference, delivery/uptake systems, sensing, energy storage and conversion devices.

In contrast, refined, processed, or functional carbon materials often do not have the requisite large surface area and structural stability [37, 38] for efficacious PB surface coverage. In the case of graphite felts, their total surface areas are not exploited fully due to the harsh conditions necessary for felt activation such as boiling in concentrated hot acids [39] or elevated temperatures [40, 41]. These treatments damage the felt fibers [42, 43]. Thus, the use of PB/felt even as ion-sieving agents is underutilized. Besides, most existing porous carbon materials are generally brittle, even in the absence of any activation protocols [44], and are even less so after thermal or acid activation. Therefore, the rarer porous yet stable carbon structures have attracted wide attention from bioengineering to electrochemical devices [37]. Next-generation electronics, energy storage/conversion devices and biological scaffolds will benefit from both the structural and functional integrity of carbon materials, especially as scaffolds in composites involving large surface area nanomaterials such as PB and PBAs.

The in situ PB formation on thermally-treated and fully-activated, high surface area and flat graphite materials is reported herein showing substantial improvements in their structural and functional integrity over comparable extent material systems. PB deposition onto the thermally-activated graphites was achieved via two new synthetic routes: for the first time, a one-solution PB formation medium with a solid steel initiator without applied potential; secondly, a solution dipping approach in high K^+ (1 M). Both protocols circumvent the intermediary acid solution phases traditionally held to be necessary for PB synthesis and stability [3]. The electrochemical and electronic properties of these PB@treated graphite materials suggest multiple electrochemical, non-electrochemical and electronic applications without compromise to the structural and functional integrity of these composites.

2 Experimental section

2.1 Sample preparation

Battery Felt SIGRACELL® GFA3 (297 × 210 × 3 mm thick) (gifts from SGL Carbon Company GmbH, Meitingen, Germany) were used as received. Pyrolytic graphite blocks, PG1 (32 ± 2 mm × 16 ± 2 mm × 0.75 ± 0.5 mm thick) (K&J Magnetics, Plumsteadville, PA, USA) were exfoliated using Scotch® tape to expose fresh pristine surfaces prior to thermal treatment and or the start of control experiments using these pristine surfaces. For pristine surfaces of GFA3, wettability was achieved by wetting in acetone and then rinsing with plenty of DI.

2.2 Thermal treatment

The thermal treatment protocol is as reported elsewhere [45]. Briefly, samples were loaded onto a ceramic block and inserted into a quartz tube furnace (Lindberg/Blue M type model, Thermo Scientific, Asheville NC, USA) pre-heated to 650 °C with both ends open to air. The contents were heated for 25 min, the tube furnace was then turned off, and the contents allowed to cool naturally.

2.3 Solution dip-method for in-situ Prussian blue nanoparticle (PBNP) formation on graphites

The PBNP were formed in situ onto the GFA3 and PG blocks by first soaking the graphites in 1 mM $(Fe(CN)_6)^{3/4-}$ (1 M KCl) (Potassium hexacyanoferrate (III) $(Fe(CN)_6)^{3/4-}$; ACS reagent, ≥ 99.0%) and potassium chloride crystal (SigmaUltra, > 99.0%, Sigma Chemical Co., St. Louis, MO, USA), prepared with DI water for 2 h. Specifically, the pristine GFA3 was wetted, prior to soaking in 1 mM $(Fe(CN)_6)^{3/4-}$ (1 M KCl)), by soaking in acetone for 5 min and rinsing with plenty of DI. The graphites were then transferred immediately into a 2 mM solution of $FeCl_2$ (iron (II) chloride, anhydrous, 99.5% [metal basis] Alfa Aesar, Haverhill, MA, USA) to form the PBNP on the graphites. The graphites-PBNP were then brought out after 2 h of sitting in the 2 mM $FeCl_2$ solution and air-dried. The air-dried graphites were then rinsed with water, acetone and plenty of water and left to air dry again. This cycle was repeated for the number of times required to obtain a given surface coverage of PBNP and or achieve specific electrochemistry signals. These reactions occurred at room temperature.

2.4 One-solution, metal-catalyzed in situ Prussian blue nanoparticle (PBNP) formation on graphites

As in above, graphite samples were soaked for 2 h in 1 mM ($\text{Fe}(\text{CN})_6^{3/4-}$ (1 M KCl)) prepared with DI water. The pristine GFA3 was wetted as described above. The soaked graphites were removed from solution and stainless steel (General UltraTech, General tools & instruments, New York, USA) run over the graphite surfaces; the stainless steel and graphites just making contact via the electrolyte (a circuit if formed at this stage), until a blue solution-graphite-stainless steel interface appeared (the yellow color of the 1 mM ($\text{Fe}(\text{CN})_6^{3/4-}$ (1 M KCl)) is changed to blue). These wet surfaces were air dried, rinsed with DI and allowed to air dry again. This process was done twice on the electrodes used for this work. These reactions occurred at room temperature.

2.5 UV-visible spectrophotometry of PBNP from the one- and two-solution methods

The PB was formed on the graphites from the one-solution, metal (steel) catalyzed reaction as explained above. When the yellow coloration of $\text{Fe}(\text{CN})_6^{3-/4-}$ turned to blue, the blue color was rinsed off the fibers into a 2 mL cuvette. More PBNP were formed and rinsed off into the cuvette until a desired volume (2 mL) was attained. This same approach was used to obtain PB solution from the two-solution method. In this case, the PB formed on the GFA3 fibers were not allowed to dry but were rinsed off into a cuvette. Their UV-Vis spectral scans, from 190 to 1100 nm, were acquired using a ThermoScientific Evolution 60S UV-Vis Spectrophotometer.

2.6 SEM imaging

Scanning electron microscope (SEM) images for the PBNP deposited on GFA3 and PG(K&J) and their corresponding controls were obtained, using beam voltages of 15 kV, via a JEOL 2010 J 200 kV Analytical TEM/STEM, with a vacuum of less than 10^{-6} Torr. Images were obtained at various magnifications.

2.7 Energy-dispersive X-ray spectroscopy (EDX)

An EDX detector fitted unto the JEOL 2010 J 200 kV Analytical TEM/STEM was used for elemental composition determination for the PBNP-graphites and their corresponding controls (graphites without PBNP). The probing beam, also used for the SEM imaging, was 15 kV.

2.8 Attenuated total reflection (ATR)-FTIR

The infrared (IR) vibrations of the cyanido groups arising from the PBNP on the graphites were obtained using the attenuated total reflection (ATR)-Fourier transform infrared (FTIR) spectroscopy technique. This analytical technique was performed using a Thermo Scientific Nicolet™ iS™ 10 FT-IR spectrometer, with the Smart iTR accessory, and the instrument interfaced to a Pentium operated desktop computer. The crystal plate for sample holding was diamond with a ZnSe lens. The samples were clamped down onto the crystal plate and lens using the pressure tower. Spectral acquisitions were averaged over 64 spectral scans to obtain a single spectrum. Spectral scans were recorded on both sides of the graphite surfaces and on a minimum of three different spots. For qualitative analysis, spectra to be compared were plotted together after manual baseline subtraction in Origin® (OriginLab Corporation) for clearer inspection.

2.9 Raman spectroscopy

Raman spectroscopy as previously described [45] utilized a WITec™ alpha300 R(aman) instrument (GmbH, Germany) with a 100-mW, frequency-doubled, Nd:YAG ($\lambda = 532.5$ nm) laser focused through a 20× Nikon objective (NA = 0.4, WD = 3.9 mm) for an excitation spot of ~ 10 μm diameter. Laser power attenuated manually to reduce fluorescence and localized thermal effects during sampling produced a final incident irradiation power of the order of 10 mW. Single spectrum “spot” scans acquired through the UHT-300 spectrometer (600 grooves/mm grating, 50- μm fiber core/collection aperture) used an Andor™ DU970 N-BV, 1600 × 200-pixel CCD array detector. Each recorded Raman spectral plot came from an average of 10 spectral accumulations at 0.50-s integration time. Optical images of the sample location were saved from each area interrogated.

2.10 X-ray photoelectron spectroscopy (XPS) and ultraviolet photoelectron spectroscopy (UPS)

To interrogate the valence states of constituent elemental compositions of the PBNP@graphite, XPS, or Electron Spectroscopy for Chemical Analysis (ESCA), measurements were carried out in an ultrahigh vacuum (UHV) environment, with a base pressure < 10^{-10} Torr. The X-ray lamp was a dual anode XR 04-548 (Physical Electronics) while the kinetic energy of the photoelectrons was measured with an Omicron EA 125 hemispherical energy analyzer having a resolution of 0.02 eV. The X-ray source used was the Al-K α source operated at 400 W. The X-ray incident angle was 54.7° and normal emission. A freshly exfoliated HOPG-ZYH sample served as the reference spectrum for

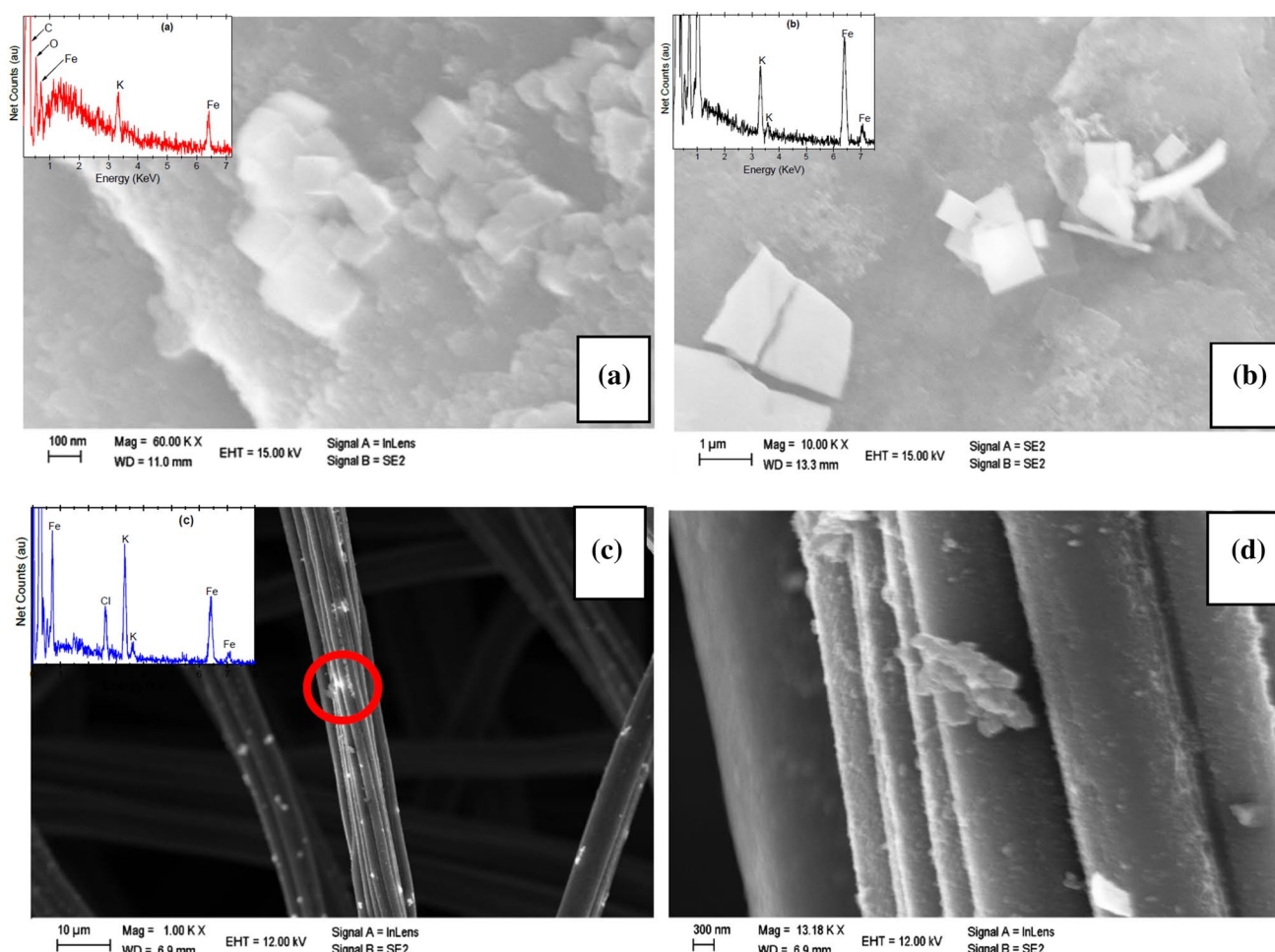


Fig. 1 Surface morphology images acquired via SEM of **a** treated GFA3-PBNP-2 \times dipped; **b** treated PG(K&J)-PBNP-6 \times dipped; and **c** GFA3-PBNP-2 \times metal-catalyzed showing the crystals glistening on various points on the graphite. **d** A higher magnification of the

red highlighted region on **c**. The images show the cube structure of Prussian blue (PB). Insets of Fig. 1: the EDS plots of (a) treated GFA3-PBNP-2 \times dipped; (b) treated-PG(K&J)-PBNP-6 \times dipped and (c) treated GFA3-PBNP-2 \times metal catalyzed

the C1s binding energy. Peak-fitting was carried out using the XPS Peak 4.1 software. The background type, using XPSPEAK41, was Shirley. The UPS spectra, used to investigate the nature of the valence electrons at the HOMO, were acquired with the same analyzer as the XPS, using both He I (21.2 eV) and He II (40.8 eV) excitation lines.

2.11 Cyclic voltammetry

Cyclic voltammetry with the various carbon materials as working electrodes operated with a VersaStat 3 potentiostat/galvanostat (Princeton Applied Research), while the counter electrode was a graphite block 99.99% pure, 40 mm \times 40 mm \times 3 mm thick (Fujiansheng, China). The reference electrode was a Ag/AgCl (3 M NaCl_(aq)) electrode (0.209 V vs. SHE) from Bioanalytical Systems Inc. (West Lafayette, IN, USA). The electrolyte was a 1 mM (Fe(CN)₆^{3-/4-} (1 M KCl)) redox-couple solution, also used for PB growth.

2.12 Data processing

The origin version 2018b[®] (version 9.55) software package was used for plotting all graphs.

3 Results and discussion

We report the synthesis and characterization of a first-time in situ PB from *only* one solution precursor (1 mM Fe(CN)₆^{3-/4-} in 1 M KCl) mediated by solid steel, and an in situ PB formation from 1 mM Fe(CN)₆^{3-/4-} (in 1 M KCl) and Fe²⁺. These PB nanoparticles (PBNP) were deposited onto thermally-activated yet stabilized graphites. The PBNP doubled the thermally-activated graphite felt capacitance without compromising their structural and functional integrity. Essentially, the steel-catalyzed and solution-dip cycles correlate electrochemically with each

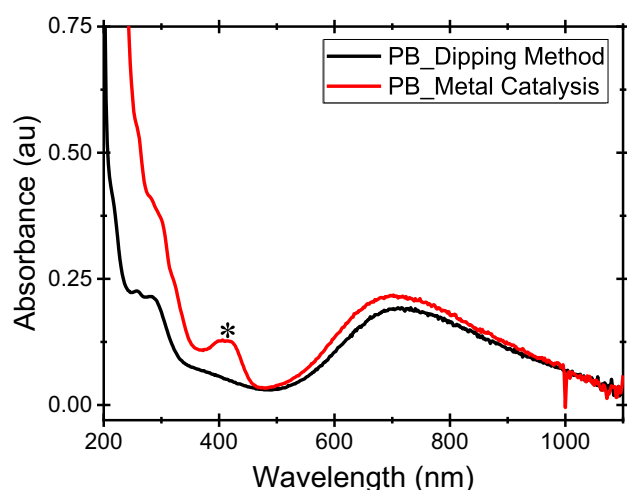


Fig. 2 The UV-visible spectroscopy of PB formed from the dipping- and metal-mediated metal catalyzes methods on treated GFA3. *The mode near 400 nm appears only for metal-catalyzed samples

other in terms of their corresponding synthesis cycles and resultant electrochemistry.

The PBNP@thermally-treated graphite SEM micrographs are shown in Fig. 1. The PB cube-like crystals are shown (Figs. 1a, b, d). Figure 1c shows the spatial distribution of the crystals on the fibers at lower magnification. On the other hand, no distinguishable morphological differences exist between the pristine GFA3 and the pristine GFA3-PBNP-2× dipped (Figs. S1 a and b), while at 2× dipped, the treated GFA3-PBNP had enough PBNP surface coverage (Fig. S1 f). Again, no distinguishable morphological differences exist between the pristine and treated GFA3, (Fig. S1a and e) to allude to morphological differences as the reason for the preferential PBNP deposition on the treated rather than the pristine GFA3. These results suggest that the thermal treatment altered the crystallinity and electronic properties of the graphites without any visible morphological changes, as earlier reported [45]. This implies that the treated GFA3 fibers are more receptive to the PBNP formation and growth (because of its enhanced crystallinity) compared to the pristine GFA3 fibers. And the same apply to the pyrolytic graphite (PG) and graphite rods. This is so because engineering the crystallinity of materials has been proved to be efficient to improve the materials' properties in many applications [46], which in this report include the adhesion of PB crystals on their graphite supports. The broader implication of these finding is that the substrate nature for PB deposition plays a role in determining the eventual chemistry of the PBNP [47, 48]. By the third dipping cycles for both treated GFA3 (Fig. S1; c and d) and pristine (Fig. S1; g and h), the cuboidal nature of the PB at the 2× dipped cycles for the treated GFA3 had given way to a more spherical PBNP as earlier

reported [49]. This is most likely due to clustering, which forced the shapes to morph from cubes into more irregular shapes.

The graphite@PBNP electron dispersive X-ray spectroscopy (EDS) results (Fig. 1 insets and S2) show elemental Fe, a key PB constituent, and sharp K^+ signals. The pristine GFA3-PBNP-2× dipped Fe signal intensity is weak (Fig. S2a) compared to those of treated GFA3-PBNP-2× dipped. These results further support the argument that treated graphite fibers are more receptive to support PB crystallization.

The PB, UV-visible spectra, from the solution dip- and metal-catalyzed methods show peaks between 250 and 300 nm and at ca. 700 nm (Fig. 2). These traits are diagnostic for PB. However, the PB from the metal catalysis had an obvious peak at 400–410 nm (*Fig. 2) not present in the PB spectrum from the solution dip method. This implies an electron-relay path difference between PB forms for charge transfer from one metal, M, to the other metal, M', in the complex. Therefore, the PB formed by metal catalysis probably has an electron travel path in its charge-transfer complex not present in that from the solution dip method. It is suggested from literature [50] that the band at ~400 nm depicts the electronic charge transfer process from iron(II) ions into high-spin sites to iron(III) ions into low-spin sites. Also, changes of this band relate to the amount of $Fe(III)_{low-spin}-CN-Fe(II)_{high-spin}$ sites, while the shoulder at 1000 nm is the forbidden transition of the above charge-transfer process.

Representative ATR-FTIR results for the PBNP@GFA3 (Figs. 3 and S3) show the ~2084 cm^{-1} peak commonly characterizing PB and its analogues. They correspond to the CN-stretching [$\nu(CN)$] in a dinuclear compound, $M-CN-M'$ [48, 51]. The magnification of this $\nu(CN)$ region is shown in Fig. 3b and suggests a PBA analogue, $Fe^{II}[Fe^{II}(CN)_6]$ [52]. The PBNP@graphite felt spectra from the solution dip methods show less interstitial OH vibrations at ca 1646 cm^{-1} . This peak is assigned to H_2O deformation or bending modes (δH_2O) [48, 53] and suggests a relatively low number concentration of coordinated water in the PB formed from this method. The PB FTIR spectrum from the one-solution method (Fig. 3c) shows $\delta(HOH)$ modes at 1595 cm^{-1} and 1673 cm^{-1} indicating lattice bound or trapped water. The peak at 2088 cm^{-1} for $\nu(CN)$ in a $M-CN-M'$ bond structure. The magnification of the regions around the $\nu(CN)$ is shown in Fig. 3d. The peaks at ca. 2088 cm^{-1} , 2137 cm^{-1} , and 2187 cm^{-1} suggest that the CN are bonded to $Fe(II)/M(II)$, $Fe(II)/M(III)$, and $Fe(III)/M(II)$, respectively [16]. These findings imply that by the reversible loss of an electron at each stage, these three oxidation states are accessed by the metal catalysis-formed PB.

The treated GFA3-PBNP and PG-PBNP micro Raman spectra (Figs. 4 and S4, respectively) show peaks

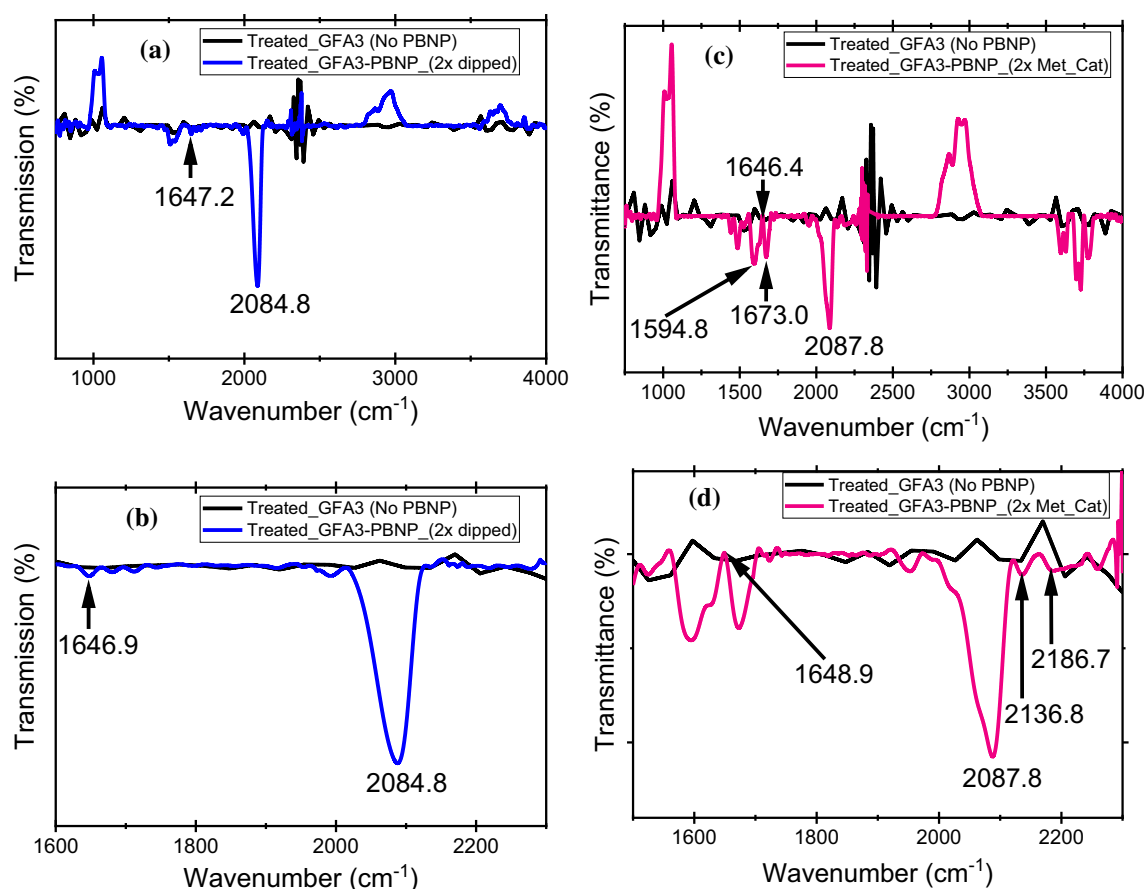


Fig. 3 ATR-FTIR spectrum of **a** treated GFA3-PBNP_(2x_dipping method), **b** magnification of the $\nu(\text{CN})$ region of **a**, **c** treated GFA3-PBNP_(2x_metal-catalyzed method), **d** magnification of the $\nu(\text{CN})$ region of **c**

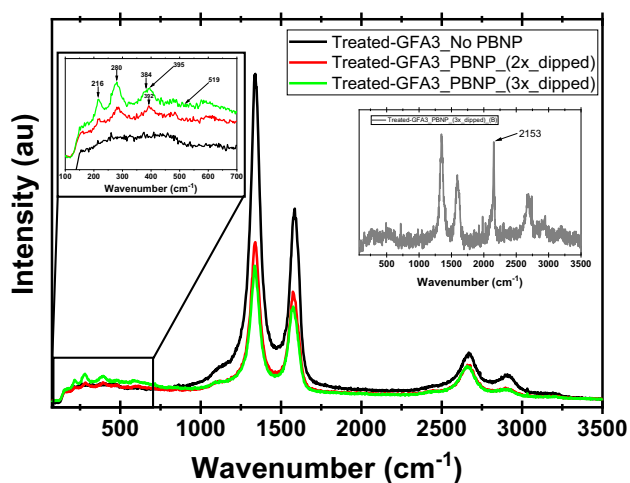


Fig. 4 Raman spectra of treated-GFA3 in the absence and presence of PBNP (2x- and 3x-dipped). Raman insets: left, the region at 700 cm^{-1} and lower shifts magnify stretching and deformation modes of the M-CN, offset on the arbitrary intensity scale for clear comparison. Right, a single carbon fiber showed the less commonly seen PB mode at 2153 cm^{-1}

at $\sim 2153\text{ cm}^{-1}$ from some sample locations, which are assigned to vibrational frequencies of the bridging CN ligands in PB [47]. These are indications of surface anchored or physisorbed CN containing groups [47, 54]. They are prominent on every scan of the PG (flat electrode) while being weak or not observable on the GFA3, appearing clearly on only one fiber probed with the focused Raman laser. This strengthens the collective points above that the substrate nature (crystallinity and morphology) contributes to defining the resultant chemistry of the PB and the PB@substrate composite.

Other metal–ligand Raman modes at less than 650 cm^{-1} are due to the presence of inorganic groups, metalorganic groups or lattice vibrations [55]. Generally, the peaks at less than 250 cm^{-1} are attributed to lattice mode vibrations, originating from crystals [56, 57], while the Raman bands between 250 and 600 cm^{-1} are from M-CN-M' vibrations. These vibrations could be resolved into $\nu(\text{MC})$, $\delta(\text{MCN})$, $\delta(\text{CMC})$, $\delta(\text{CMN})$ and combination modes, which all appear in the region below 550 cm^{-1} [56]. These vibrational modes indicate the presence of PB (Figs. 4 and S4). For example, the treated GFA3-PBNP samples spectra have ~ 384

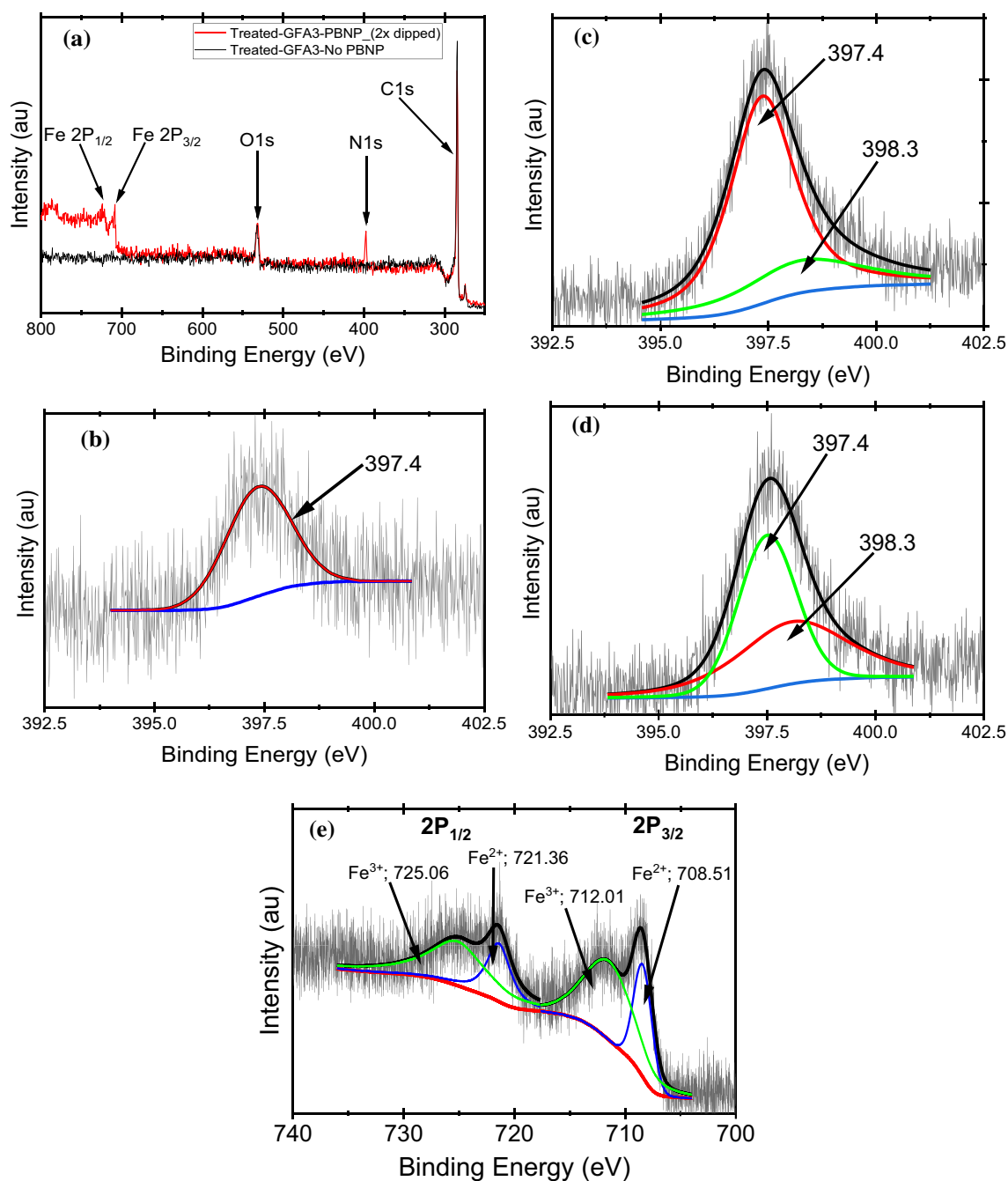


Fig. 5 **a** Wide angle (“survey”) XPS spectra of treated GFA3-PBNP-2x dipped and treated GFA3-No PBNP; High resolution XPS spectra of **b** N1s in treated PG(K&J)-PBNP-3x dipped; **c** N1s in

treated GFA3-PBNP-2x dipped; **d** N1s in treated GFA3-PBNP-2x Met Cat; and **e** Fe2P in treated GFA3-PBNP-2x dipped

and $\sim 401\text{ cm}^{-1}$ peaks, corresponding to the in-plane E_{2g}^1 and the out-of-plane A_{1g} modes, respectively. Also, the 519 cm^{-1} (E_{1g}) modes are evident. These results suggest octahedral-coordinated ligand-to-metal centers, stacked-up in a layered fashion [58–61].

Electrochemical spectroscopy for chemical analysis (ESCA), or XPS, was used to determine both the chemical composition and spin states of the PB elemental constituents. The wide angle XPS (“survey”) results of treated GFA3-PBNP-2x dipped (Fig. 5a) and other treated graphite-PBNP (Fig. S5a and b) show elemental Fe and N not present in their controls. At high resolution XPS scan (Fig. 5b–d),

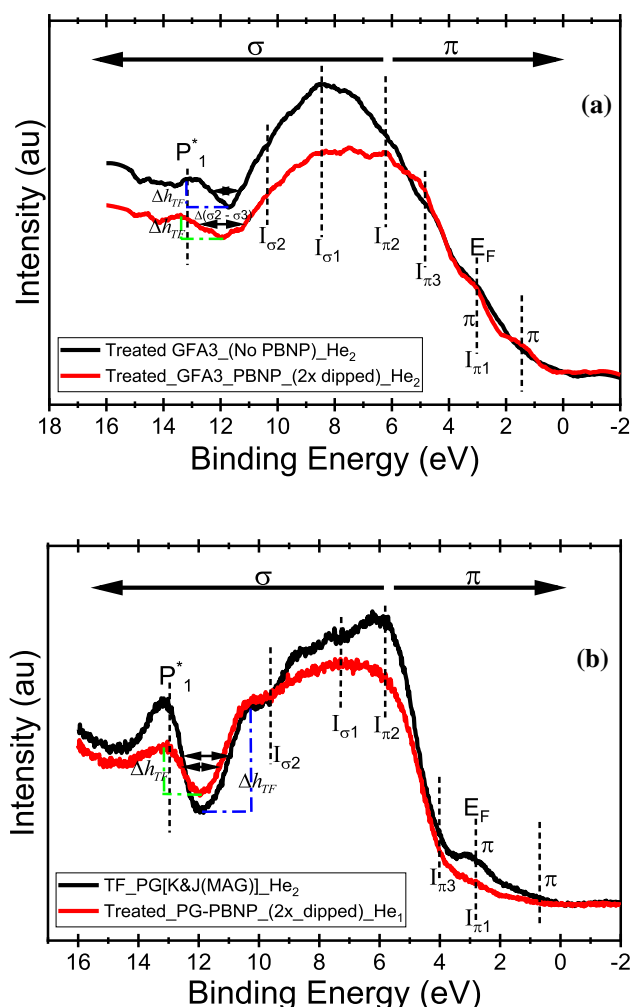


Fig. 6 **a** the valence band spectra at the HOMO obtained from the He₂ and **b** He₁ lines of the treated GFA3-PBNP-2× dipped and its control, treated GFA3 (no PBNB) with highlights of the various intensity bands

their Fe nitrides binding energy is at ~397 eV, indicating that the PB nitrogen is present as a metal-bound nitride [62]. The metal in this case been Fe. However, in addition to the 397.4 eV peaks of the nitrides of the treated GFA3-PBNP, there is another peak at ~398.1 eV. In the M-CN-M' charge transfer complex, overlap of the molecular orbitals of the cyanide complex clusters with the atomic orbitals of K do occur [63]. Such interaction has been reported of CN clusters with cations in its vicinity to result in a XPS metal-nitride peak near 398 eV [64]. Thus, for the T-GFA3-PBNP-2× dipped, the ratio of the areas of the peaks at 397.4 eV to that of 398.2 eV is ~3, while the ratio for the T-GFA3-PBNP-2× metal catalysis is approximately 1. These ratio values suggest that the 398.2 eV conformation is a minor contributor to the overall state of the N-metal interaction for PB in the solution dip method but is a major conformational state for PB from metal catalysis. An implication

of this finding is that the CN clusters associated with K⁺ in the PB from solution dip method is a minor and less likely pathway for charge delocalization along the charge-relay complex of its metal-cyanide. On the other hand, these CN clusters-K⁺ association would be a probable pathway for charge delocalization along the M-CN-M' of the PB from metal catalyzes. Additionally, Fe in the PB matrix contains both divalent and trivalent states, in integer proportions, as shown in the representative Fe 2P states in the treated GFA3-PBNP-2× dipped (Figs. 5e and S5c). Thus, the actual structure is an Fe^{II}-CN-Fe^{III} dinuclear compound with a Fe²⁺/Fe³⁺ ~ 1 or 2.

To understand the impact of the PBNP on the electronic properties of the thermally-treated graphite, graphite-PBNP Ultraviolet Photoelectron Spectroscopy (UPS) data were compared with those of the treated graphite (no PBNP) (Fig. 6). The aim was to investigate if, and how, the PB interaction with the treated graphite surfaces distort (or leave unchanged) the valence electron (HOMO level) properties of the treated graphites. To interrogate these electronic properties, an analysis of the π -band peak intensities over those of the σ bands (Fig. 6) were calculated as already explained elsewhere [45]. The results show that treated graphites and graphite-PBNP had about the same signal intensities and peak values up to the E_F region. However, the graphite-PBNP I_{π2}/I_{σ1} was higher than that without PBNP. This suggests an enhancement by specific heat-treatment of π over σ character (Fig. 6a). Additionally, the difference between the two σ bonds, $\Delta(\sigma2-\sigma3)$, is greater for the treated graphite-PBNP than without PBNP, indicative of a stronger σ -bond interaction facilitated by the PB, while the π -bond nature of the PB@graphite is enhanced. This enhancement of π over σ bonds is a common trait of conjugation and conductivity [65]. On the other hand, the He₁ probed spectrum (Fig. 6b) suggests the reverse is true for thermally-treated graphite having a slightly enhanced π over σ trait (I_{π2}/I_{σ1}) and a shorter $\Delta(\sigma2-\sigma3)$ distance. However, the treated graphite with PB has a smaller energy well depth, Δh , than without PB, reflecting a stronger σ -bond interaction in terms of bond strength [66], stability [67], and molecular size [68]. In summary, the electronic properties of the PBNP@treated graphite-2× dipped are similar to those of the treated graphite without PBNP. The UPS of the treated PG and PG-PBNP (Fig. S6) show a similar trend.

The UPS data suggest that the 2× dipping cycles employed for PB formation did not perturb or disrupt the electronic nature of the treated graphite nor, by extension, of the PB from the metal-catalyzed phase since the UPS from both synthesis cycles are very similar. This suggests, as was earlier postulated, a Hubbard-type model characteristic [69] conferred by the thermal treatment protocol on the graphites. Briefly, the Hubbard model implies that the electronic structure of the treated structure is

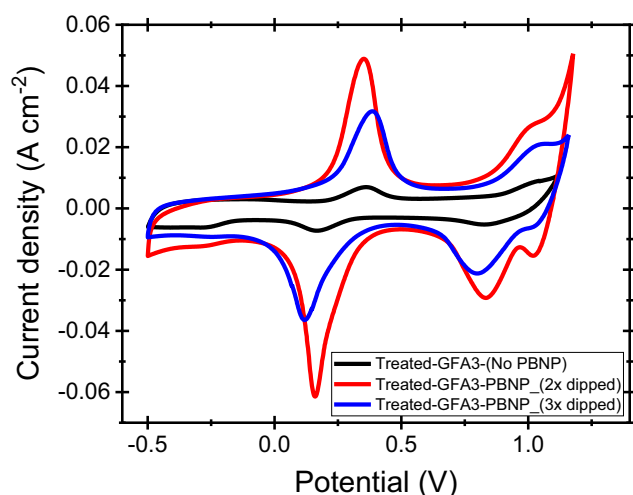


Fig. 7 The CV in 1 mM Fe(CN)₆^{3-/4-} of treated-GFA3 (No PBNP), treated-GFA3-PBNP-2× dipped and treated-GFA3-PBNP-3× dipped. $v = 0.05 \text{ V s}^{-1}$

Table 1 Capacitance (mF cm^{-2}) and peak potential differences (ΔE_p (mV)) of pristine and treated GFA3 in the presence and absence of PBNP, deposited via different dipping cycles ($n=3$ for each electrode type)

Electrode type	ΔE_p (mV) @ $v = 0.05 \text{ V s}^{-1}$	Capacitance (mF cm^{-2})
Pristine GFA3	179 ± 27	8.5 ± 1.0
Pristine GFA3-PBNP_(2× dipped)	158 ± 2	10.7 ± 0.5
Pristine GFA3-PBNP_(3× dipped)	299 ± 2	15.6 ± 1.2
Treated GFA3	209 ± 17	70.6 ± 4.0
Treated GFA3-PBNP_(2× dipped)	215 ± 39	137.4 ± 7.0
Treated GFA3-PBNP_(3× dipped)	262 ± 18	125 ± 7.9

correlated (cannot be explained by a single electron wavefunction) and non-perturbative (not disrupted) even by non-native surface properties [70]. In this case, it is the PB on the graphite surfaces. One of the implications of these findings is that the electrochemistry of the heat-treated graphites could be improved upon without repercussions on the integrity of its electronics and other electronics-dependent properties.

The CVs in 1 mM Fe(CN)₆^{3-/4-} of treated (Fig. 7) and pristine GFA3 (Fig. S7) with and without PBNP show that thermal treatment improved both the kinetics and capacitance even without PBNP. This improvement is due to the increased crystallinity and proper electronic tuning of the treated graphite as discussed [45]. In the presence of PBNP (2× and 3× dipped), the treated GFA3 capacitance doubled while those of the pristine GFA3-PBNP nearly doubled by the third dipping cycle (Table 1). However, the pristine GFA3-PBNP-3× dipped capacitance is eight times less to the treated GFA3-PBNP-3× dipped, even though their

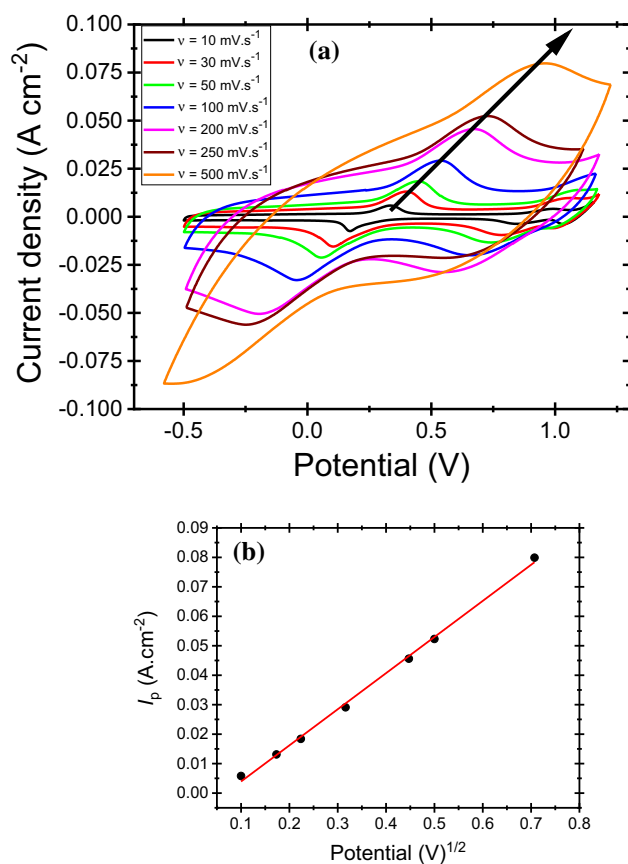


Fig. 8 **a** The CV in 1 M KCl of the treated-GFA3-PBNP-2× dipped and at various scan rates from 10 to 500 mV. **b** the peak current density of the various scan rates, showing the diffusion-controlled kinetics of the treated-GFA3-PBNP-2× dipped

morphologies are very similar (Fig. S1; c and d). The explanation for these discrepancies in the PB carrying-capacities on the treated and pristine graphites lies with the treated GFA3 crystalline nature, which is also responsible for its capacitance increase by making available more usable and more receptive surfaces for PB formation. This contrasts with the less crystalline and less receptive pristine GFA3 surfaces. In other words, the PB only optimizes the surfaces presented to it.

Again, as in above, the substrate nature contributes in defining the resultant PB and or PB@graphite chemistry [47, 48]. Additionally, the consistency of the PB chemistry on both the treated and pristine GFA3 indicates the homogeneity of these PB forms on the carbon types employed. The thermally treated graphite-PBNP (3× dipped) capacitance was slightly less than after only two dips. This slight decrease may come from PB stacking so that agglomeration of the octahedral structures (SEM images in Figs. S1; g and h) could have introduced more defects, thus decreasing the volume carrying capacity of the PB. Irregular to spherical PB agglomerates have more disordered

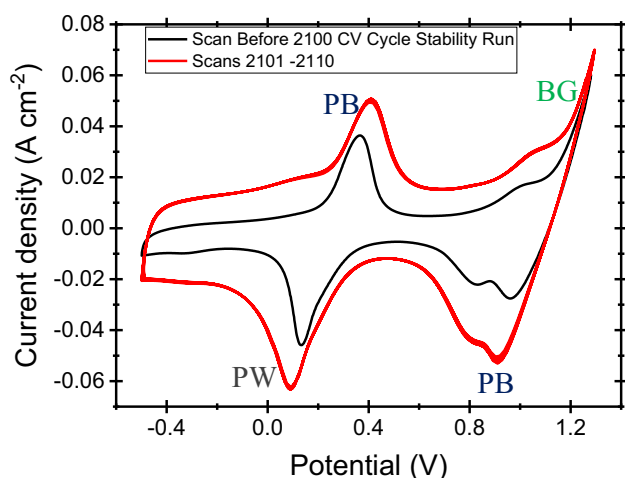


Fig. 9 Cycle stability test of the treated GFA3-PBNP (2× dipped) in 1 mM $\text{Fe}(\text{CN})_6^{3-/4-}$ (1 M KCl), from -0.5 to 1.3 V. The cyclic voltammograms before and after 2100 consecutive cycles as stability indicator

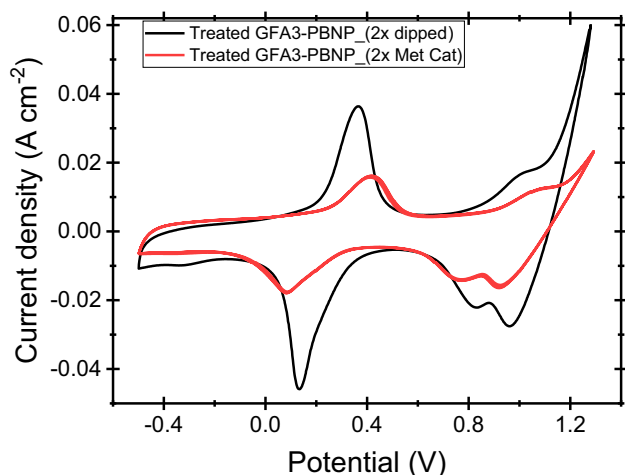
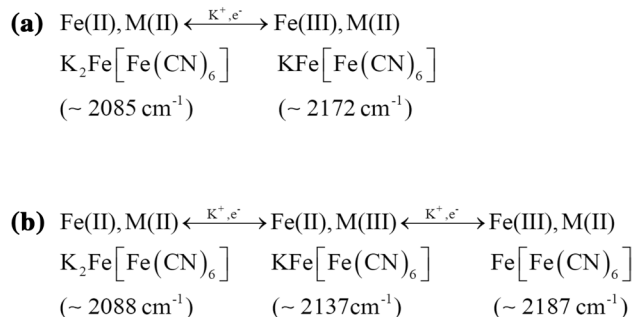


Fig. 10 The cyclic voltammetry of PBNP from metal catalysis (2× catalyzed) and from the solution dip method (2× dipped) on treated GFA3. The CV was in 1 mM $\text{Fe}(\text{CN})_6^{3-/4-}$ (1 M KCl) and $v=0.05 \text{ V s}^{-1}$

vacancies and smaller specific surface area compared to cubic PB [71]. This could explain the widening cathodic and anodic peak potentials of the treated GFA3-PBNP-3× dipped, reflected also as increased ΔE_p (slower kinetics).

The PBNP@treated graphite CVs at various scan rates are shown in Fig. 8a. A plot of their anodic peak current densities to its corresponding scan rates indicates diffusion-controlled kinetics at these peaks (Fig. 8b). The poor cycle stability of PB [1, 35], and instability in neutral and alkaline solutions [47, 48], impose constraints on the CV cycle numbers that could be performed on PB and

$$[\text{M} / \text{Fe} = 1]$$



Scheme 1 Electron relay pathway for the charge-transfer complexes formed by the **a** solution dip and **b** metal-catalyzed methods for PB formation. Scheme modified from Ref. [16]

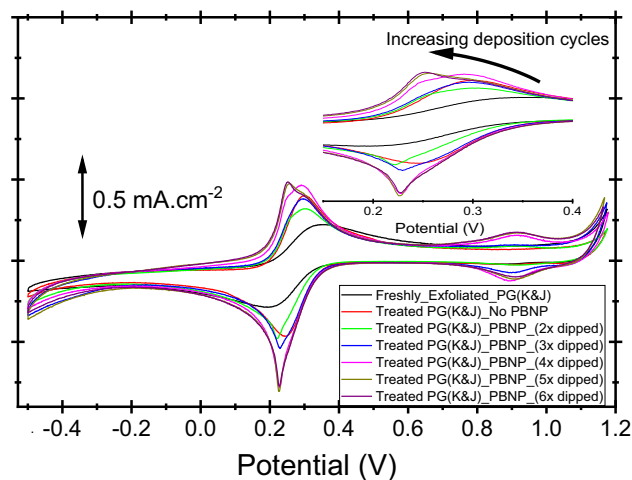


Fig. 11 The CV in 1 M KCl of freshly exfoliated, treated PG(K&J) and treated PG(K&J)-PBNP at various dipping cycles of the synthesis reagents. Insert is the magnification of the area around the cathodic and anodic peak potentials

its composites. For example, a comparable work involving graphite fibre-Pt-PB with CV cycles of 150 has been reported [72]. To investigate the PB@treated felts cycle stability, 2100 CV cycles ran from 1.3 to -0.5 V in 1 M KCl. Initial and final CV curves (2100 cycles) show that the PB@treated felts are highly consistent against these cycling conditions (Fig. 9).

The CV stabilities across the entire potential window range, -0.5 to $+1.3$ V (Fig. 9), indicate Prussian white (PW at approx. -0.4 V) to PB at ~ 0.4 V (and vice versa) and PB to Berlin green (BG at ~ 1.3 V) (reversibly) transition stabilities [72]. These stabilities show the PB-zeolite nature stabilities to the constant motions of deintercalating/intercalating ions during the CV cycles. Thus, our results show highly

Table 2 Cyclic voltammetry of pristine PG, treated PG and treated PG-PBNP at various deposition cycles of PBNP on the treated PG (n=3)

Electrode	ΔE_p (mV) @ $v=0.05 \text{ V s}^{-1}$
Freshly exfoliated PG	194 ± 23
Treated PG (no PBNP)	59 ± 2
Treated PG-PBNP_(2× dipped)	75 ± 1
Treated PG-PBNP_(3× dipped)	66 ± 1
Treated PG-PBNP_(4× dipped)	61 ± 2
Treated PG-PBNP_(5× dipped)	28 ± 3
Treated PG-PBNP_(6× dipped)	22 ± 2

porous and stable PB structures, unlike carbon materials in general [44]. Besides, such low-defect PB with high capacity, strong rate capability and long cycle life have been associated with PB synthesis in concentrated K^+ [36], such as was used in this work.

The electrochemistry of PB from the metal catalysis correlates strongly with those of the solution dip-cycles (Fig. 10), even though their UV–visible and IR spectra suggests that the charge transfer between the metals, M and M' in the complex, M-CN-M' are via different electron relay paths. The PB XPS (Fig. 5) shows a Fe^{II} -CN- Fe^{III} dinuclear compound with $Fe^{2+}/Fe^{3+} \sim 1$ or 2. PB with an M/Fe = 1 or integers indicate absence of dangling bonds or defect-free lattices, where M is a transition metal with +2 oxidation state and Fe is in the +3 oxidation state [16]. Thus, their CV data imply defect-free PB lattices.

Also, from the UV–Vis, FTIR, and high resolution XPS N1s fitted spectra, the metal-catalyzed PB form has one intermediary path of electron travel from the metals M to M' in the M-CN-M' complex and more interstitially coordinated water to that from the dipping method. Scheme 1 shows

the paths to accessible oxidation states and K^+ coordination during a charge-relay process.

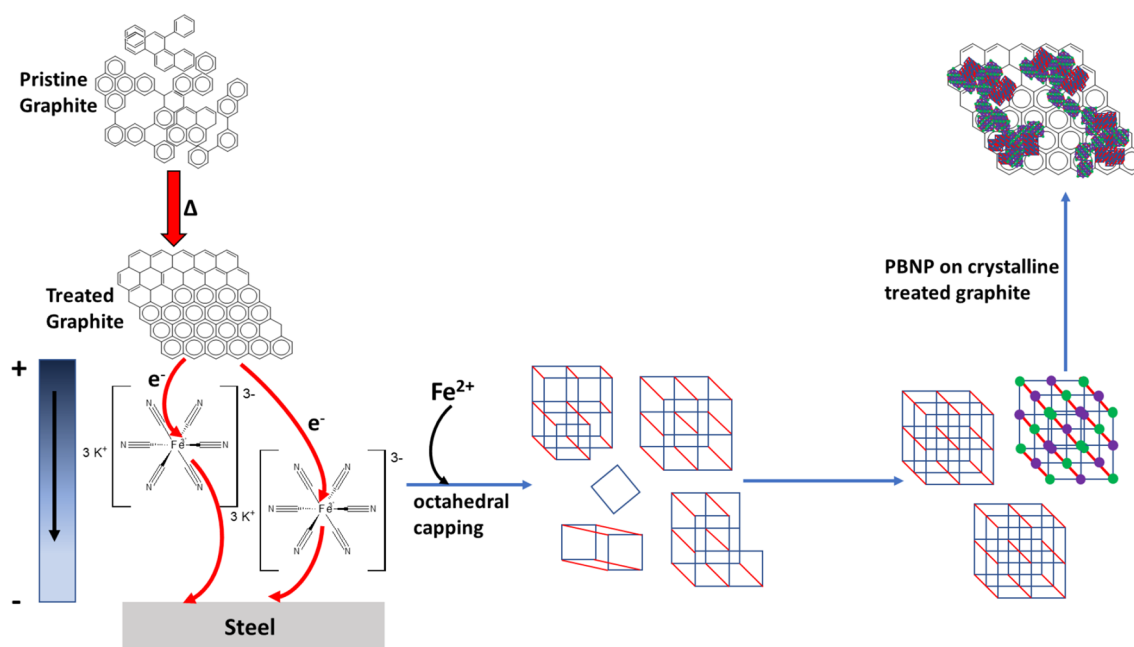
The PG electrode CVs and highlights on their peak potential regions are shown in Fig. 11 (and Fig. S8 for the treated graphite rod@PBNP). For example, the pristine electrode had ΔE_p of 194 ± 23 mV and 59 ± 2 mV for the treated PG. The treated PG-PBNP-2× dipped rose to 75 ± 1 mV, then dropped after subsequent dips (Table 2).

The ΔE_p increase (slow kinetics) before a decrease highlights the poor conductivity of PB [34], mainly because of large interstitial voids [4], coordination of the metals to water [73], and/or even defect or disordered valences [71]. However, since further PB formation and deposition cycles decreased the ΔE_p , it implies that the formed PB have very little or no defect valences [36] so that further stacking of the PB zeolite structures resulted in coordinated and interacting structures with sufficient conductivities to decrease the ΔE_p . This inference is supported by the work that suggests that zeolite-like PB with soluble K^+ (for example, as seen from our EDS results; Fig. 1 insets and S2) usually results in less defective PB with large crystallite sizes [71] (as seen, for example, from our SEM; Figs. 1 and the XPS Fe^{2+}/Fe^{3+} which suggests less defective PB) and less water within its lattices [29]. This could account for the apparent lack of $\nu(OH)$ in the PBNP@graphite IR spectra (Figs. 3 and S3). The K^+ located inside the lattice cavities [73] serves as a PB coordinating unit, increasing the PB conductivity on the graphites. For comparison, the two-solution dip method is more than 5 times more efficient than a similar synthetic path to deposit PB on porous alumina [74]. The PBNP@treated PGs and PBNP@treated graphite rods have comparable electrochemistry to PB on Pt [72] or Au [75, 76], making the PBNP@treated graphites cheap and commercially feasible alternatives to these other expensive ones. These findings are important to sensing, ion selectivity for

Table 3 Comparison of the capacitance of PB and analogous structures of PB on different materials

Material	Electrolyte	i (mA cm ⁻²)	v (V s ⁻¹)	Capacitance (mF cm ⁻²)	Potential window (V)	References
Treated GFA3-PBNP	1 M KCl	13.74 ± 3	0.05	137.4 ± 7.0	1.8	This work
Mo-PB	0.5 M K_2SO_4	10	0.05	100	1.8	[77]
CoHCF	0.5 M Na_2SO_4	16	0.05	160	1.2	[30]
FTO-PB	1 M KCl	0.8	0.02	20	0.9	[4]
Carbon paper-PB	1 M KNO_3	0.4	0.0005	400	1.35	[78]
PB/N-doped Porous Carbon	1 M KNO_3	40	0.05	400	1.0	[79]
PB-composite	1.0 M Na_2SO_4	0.5	0.001	250	1.6	[36]
PB-composite	0.5 M K_2SO_4	22.5	0.05	225	1.2	[80]
MnO_x @MHCF	1.0 M Na_2SO_4		0.05	175	0.8	[81]
PB-MnHCF	0.10 M KNO_3	0.40	0.05	4	1.0	[82]
PtCu ₃ nanocages	0.1 M $HClO_4$	2.0	0.02	50	1.20	[83]

These parameters are calculated off cyclic voltammogram data



Scheme 2 Depiction of the mechanism of PB formation from a galvanic series-based circuit formed by the $\text{Fe}(\text{CN})_6^{3-/4-}$, graphite and steel

capture/release systems, energy storage and conversion systems.

A comparison of the capacitance and potential windows of PB/PB-composites and similarly structured analogues (Table 3) suggests that the PB@thermally treated graphite reported herein has very competitive potential window and capacitance. This is unlike other PBs in the table that may have appreciably high capacitance but very limiting potential windows, and vice versa. Having high capacitance with a low potential window (and vice versa) severely limits the functional ranges and restricts application feasibility of such PB-composites.

3.1 Metal-catalyzed PBNP on graphite

The PB CVs from the metal catalyzed and solution dip methods have similar electrochemistry at the same synthesis cycles (see, for example, Fig. 10). This suggests that about the same cation and anion concentrations were involved at every stage of both PB synthetic pathways. A common route for free or liberated iron in solution would be Fe^{3+} from ferri-cyanide solution decomposition [84]. The liberated Fe^{3+} can then react with the ferri-cyanide to form PB. However, this pathway cannot account for the PB formation since no PB formed by either soaking the graphites in $\text{Fe}(\text{CN})_6^{3-/4-}$ or by running CVs of these electrodes in $\text{Fe}(\text{CN})_6^{3-/4-}$. It is postulated that a closed electrochemical circuit is formed between the graphite, 1 mM $\text{Fe}(\text{CN})_6^{3-/4-}$ (1 M KCl) and the stainless steel (all three components being congruous at the instant of PB formation).

The stainless steel is lower on the galvanic or electropotential series to the graphite and would serve as the anode in this galvanic circuit. In this circuit, the graphite (cathode) loses electrons en route to the anode. However, the electrolyte captures these electrons, disrupting the octahedral structure of the $\text{Fe}(\text{CN})_6^{3-/4-}$ to liberate Fe^{3+} . The liberated Fe^{3+} is immediately reduced to Fe^{2+} by more in-streaming electrons from the graphite. The Fe^{2+} then reacts with the $\text{Fe}(\text{CN})_6^{3-/4-}$, closing the vertices or “capping” the octahedral structure of the $\text{Fe}(\text{CN})_6^{3-/4-}$ to form PB (Scheme 2).

4 Conclusions

Since most porous carbon materials are generally brittle [44], and even more so after thermal or acid activation [39–41], the PBNP@treated graphite composites is not commonly reported. The present work shows highly porous and stable PBNP composited on thermally-treated and activated graphite materials. These PBNP on fully-activated, high surface area graphite materials without compromise to their structural and functional integrity, meet the demands for the next generation electronics, energy storage/conversion devices and biological scaffolds. These newly stable structure–function properties of PBNP on graphites are unlike carbon materials in general [44]. An important implication of the present work is that the synthesis method influences the intermediacy of electron travel in the M-CN-M' charge transfer complex. Also, the substrate nature for PB deposition plays a

critical role in the eventual chemistry of the PB and PB@ substrate. The PBNP@treated graphite felts have a very competitive potential window, the highest capacitance in 1 mM $\text{Fe}(\text{CN})_6^{3-/4-}$ (1 M KCl), remained stable for over 2100 CV cycles in 1 M KCl solution, and its synthesis method some 5 times more efficient than a similarly reported method [74]. Moreover, these new synthesis methods are green, avoiding harsh or corrosive solvents and require no charge or voltage applications to achieve their synthesis. Also, these methods circumvent the traditionally required low pH phases for PB synthesis. Their electrochemistry suggests competitive material behavior for applications in aqueous-based energy storage and conversion devices.

The current findings highlight carbon materials, with structural and functional integrity, and low-cost, for energy storage/conversion devices such as, in this case, aqueous-based supercapacitors, batteries and fuel cells. Also, the PBNP@treated carbon felt capacitance increases, relative to the bare thermally-treated felt itself, make these composites practical for ion selectivity in capture/release systems. The treated PG and graphite rod electrochemistry are now feasible substitutes not just for Au and Pt in electrochemical and electronic devices but also for potential Au-PBNP and Pt-PBNP replacements. Future work would explore PBNP@thermally-treated graphite applications for sensors and other applications commonly associated with Au- and Pt-PBNP composite electrodes.

Acknowledgements OCN appreciates research funding from the College of Science and the College of Graduate Studies Deans' Offices and the Department of Chemical and Materials Engineering (UI). He also recognizes the Integrated Research and Innovation Center (IRIC) at the University of Idaho. L. Scudiero of the Department of Chemistry and Material Science and Engineering Program at Washington State University is warmly thanked for helpful discussions on photoelectron spectroscopy.

Compliance with ethical standards

Conflict of interest The authors declare no conflict of interest.

References

- Koshiyama T, Tanaka M, Honjo M, Fukunaga Y, Okamura T, Ohba M (2018) Direct synthesis of Prussian blue nanoparticles in liposomes incorporating natural ion channels for Cs^+ adsorption and particle size control. *Langmuir* 34:1666–1672
- Cvrtila I, Stilianovic V (2017) New tricks by old anions: hydrogen bonded hexacyanoferrous anionic networks. *Cryst Growth Des* 17:6793–6800
- Karyakin A (2008) Chemical and biological sensors based on electroactive inorganic polycrystals. In: Zhang X, Ju H, Wang J (eds) *Electrochemical sensors, biosensors and their biomedical applications*. Elsevier, Amsterdam, pp 411–439
- Morant-Giner M, Sanchis-Gual R, Romero J, Alberola A, García-Cruz L, Agouram S, Galbiati M, Padial NM, Waerenborgh JC, Martí-Gastaldo C et al (2018) Prussian blue@ MoS_2 layer composites as highly efficient cathodes for sodium- and potassium-ion batteries. *Adv Funct Mater* 28:1706125
- Buser HJ, Ludi A, Schwarzenbach D, Petter W (1977) The crystal structure of Prussian blue: $\text{Fe}_4[\text{Fe}(\text{CN})_6]_3 \cdot x\text{H}_2\text{O}$. *Inorg Chem* 16:2704–2710
- Pyrasch M, Toutianoush A, Jin W, Schnepf J, Tiede B (2003) Self-assembled films of Prussian blue and analogues: optical and electrochemical properties and application as ion-sieving membranes. *Chem Mater* 15:245–254
- Chen R, Tanaka H, Kawamoto T, Asai M, Fukushima C, Kurihara M, Ishizaki M, Watanabe M, Arisaka M, Nankawa T (2013) Thermodynamics and mechanism studies on electrochemical removal of cesium ions from aqueous solution using a nanoparticle film of copper hexacyanoferrate. *ACS Appl Mater Interfaces* 5:12984–12990
- Thammawong C, Opaprakasit P, Tangboriboonrat P, Sreearunothai P (2013) Prussian blue-coated magnetic nanoparticles for removal of cesium from contaminated environment. *J Nanopart Res* 15:1689
- Catala L, Mallah T (2017) Nanoparticles of Prussian blue analogs and related coordination polymers: from information storage to biomedical applications. *Coord Chem Rev* 346:32–61
- Vipin AK, Fugetsu B, Sakata I, Isogai A, Endo M, Li M, Dresselhaus MS (2016) Cellulose nanofiber backbone Prussian blue nanoparticles as powerful adsorbents for the selective elimination of radioactive cesium. *Sci Rep* 6:37009
- Jang S-C, Hong S-B, Yang H-M, Lee K-W, Moon J-K, Seo B-K, Huh Y, Roh C (2014) Removal of radioactive cesium using Prussian blue magnetic nanoparticles. *Nanomaterials* 4:894–901
- Qin Z, Li Y, Gu N (2018) Progress in applications of Prussian blue nanoparticles in biomedicine. *Adv Healthc Mater* 7:1800347
- DeLongchamp DM, Hammond PT (2004) High-contrast electrochromism and controllable dissolution of assembled Prussian blue/polymer nanocomposites. *Adv Funct Mater* 14:224–232
- Schmidt DJ, Cebeci FÇ, Kalcioğlu ZI, Wyman SG, Ortiz C, Van Vliet KJ, Hammond PT (2009) Electrochemically controlled swelling and mechanical properties of a polymer nanocomposite. *ACS Nano* 3:2207–2216
- Wood KC, Zacharia NS, Schmidt DJ, Wrightman SN, Andaya BJ, Hammond PT (2008) Electroactive controlled release thin films. *Proc Natl Acad Sci* 105:2280–2285
- De Tacconi NR, Rajeshwar K, Lezna RO (2003) Metal hexacyanoferrates: electrosynthesis, in situ characterization, and applications. *Chem Mater* 15:3046–3062
- Wang H, Huang Y (2011) Prussian-blue-modified iron oxide magnetic nanoparticles as effective peroxidase-like catalysts to degrade methylene blue with H_2O_2 . *J Hazard Mater* 191:163–169
- Haghighi B, Hamidi H, Gorton L (2010) Electrochemical behavior and application of Prussian blue nanoparticle modified graphite electrode. *Sens Actuators B Chem* 147:270–276
- Peng X, Wang R, Wang T, Yang W, Wang H, Gu W, Ye L (2018) Carbon dots/Prussian blue satellite/core nanocomposites for optical imaging and photothermal therapy. *ACS Appl Mater Interfaces* 10:1084–1092
- Zhou J, Li M, Hou Y, Luo Z, Chen Q, Cao H, Huo R, Xue C, Sutrisno L, Hao L et al (2018) Engineering of a nanosized biocatalyst for combined tumor starvation and low-temperature photothermal therapy. *ACS Nano* 12:2858–2872
- Fu G, Liu W, Li Y, Jin Y, Jiang L, Liang X, Feng S, Dai Z (2014) Magnetic Prussian blue nanoparticles for targeted photothermal therapy under magnetic resonance imaging guidance. *Bioconjug Chem* 25:1655–1663
- Kim T, Lemaster JE, Chen F, Li J, Jokerst JV (2017) Photoacoustic imaging of human mesenchymal stem cells labeled

- with Prussian blue–poly(L-lysine) nanocomplexes. *ACS Nano* 11:9022–9032
23. Zakaria MB, Chikow T (2017) Recent advances in Prussian blue and Prussian blue analogues: synthesis and thermal treatments. *Coord Chem Rev* 352:328–345
 24. Patra CR (2016) Prussian blue nanoparticles and their analogues for application to cancer theranostics. *Nanomedicine (Lond)* 11:569–572
 25. Zhou B, Jiang BP, Sun W, Wei FM, He Y, Liang H, Shen XC (2018) Water-dispersible Prussian blue hyaluronic acid nanocubes with near-infrared photoinduced singlet oxygen production and photothermal activities for cancer theranostics. *ACS Appl Mater Interfaces* 10:18036–18049
 26. Peng Y, Li B, Wang Y, He X, Huang J, Zhao J (2017) Prussian blue: a potential material to improve the electrochemical performance of lithium–sulfur batteries. *ACS Appl Mater Interfaces* 9:4397–4403
 27. Ji Z, Han B, Liang H, Zhou C, Gao Q, Xia K, Wu J (2016) On the mechanism of the improved operation voltage of rhombohedral nickel hexacyanoferrate as cathodes for sodium-ion batteries. *ACS Appl Mater Interfaces* 8:33619–33625
 28. Zhang C, Xu Y, Zhou M, Liang L, Dong H, Wu M, Yang Y, Lei Y (2017) Potassium Prussian blue nanoparticles: a low-cost cathode material for potassium-ion batteries. *Adv Funct Mater* 27:1604307
 29. Qian J, Wu C, Cao Y, Ma Z, Huang Y, Ai X, Yang H (2018) Prussian blue cathode materials for sodium-ion batteries and other ion batteries. *Adv Energy Mater* 8:1702619
 30. Zhao F, Wang Y, Xu X, Liu Y, Song R, Lu G, Li Y (2014) Cobalt hexacyanoferrate nanoparticles as a high-rate and ultra-stable supercapacitor electrode material. *ACS Appl Mater Interfaces* 6:11007–11012
 31. Zhang M, Hou C, Halder A, Ulstrup J, Chi Q (2017) Interlocked graphene-Prussian blue hybrid composites enable multi-functional electrochemical applications. *Biosens Bioelectron* 89:570–577
 32. Wang X, Zou L, Fu H, Xiong Y, Tao Z, Zheng J, Li X (2016) Noble metal-free oxygen reduction reaction catalysts derived from Prussian blue nanocrystals dispersed in polyaniline. *ACS Appl Mater Interfaces* 8:8436–8444
 33. Murase R, Leong CF, D'Alessandro DM (2017) Mixed valency as a strategy for achieving charge delocalization in semiconducting and conducting framework materials. *Inorg Chem* 56:14373–14382
 34. Bocharova V, Gorodyska G, Kiriya A, Stamm M, Simon P, Mönch I, Elefant D, Lou X, Stoffelbach F, Detrembleur C et al (2006) Synthesis and deposition of water-dispersed Prussian blue nanocrystals on polymers and CNTs. *Prog Colloid Polym Sci* 132:161–167
 35. Xu Y, Zheng S, Tang H, Guo X, Xue H, Pang H (2017) Prussian blue and its derivatives as electrode materials for electrochemical energy storage. *Energy Storage Mater* 9:11–30
 36. Wu X, Luo Y, Sun M, Qian J, Cao Y, Ai X, Yang H (2015) Low-defect Prussian blue nanocubes as high capacity and long life cathodes for aqueous Na-ion batteries. *Nano Energy* 13:117–123
 37. Ni N, Barg S, Garcia-Tunon E, MacUl Perez F, Miranda M, Lu C, Mattevi C, Saiz E (2015) Understanding mechanical response of elastomeric graphene networks. *Sci Rep* 5:13712
 38. Qiu L, Liu JZ, Chang SLY, Wu Y, Li D (2012) Biomimetic superelastic graphene-based cellular monoliths. *Nat Commun* 3:1241
 39. Sun B, Skyllas-Kazakos M (1991) Chemical modification and electrochemical behaviour of graphite fibre in acidic vanadium solution. *Electrochim Acta* 36:513–517
 40. Pupkevich V, Glibin V, Karamanov D (2007) The effect of activation on the electrochemical behaviour of graphite felt towards the $\text{Fe}^{3+}/\text{Fe}^{2+}$ redox electrode reaction. *Electrochim Commun* 9:1924–1930
 41. Sun B, Skyllas-Kazakos M (1992) Modification of graphite electrode materials for vanadium redox flow battery application—I. Thermal treatment. *Electrochim Acta* 37:1253–1260
 42. Trogadas P, Taiwo OO, Tjaden B, Neville TP, Yun S, Parrondo J, Ramani V, Coppens MO, Brett DJL, Shearing PR (2014) X-ray micro-tomography as a diagnostic tool for the electrode degradation in vanadium redox flow batteries. *Electrochim Commun* 48:155–159
 43. Lim TH, Yeo SY (2017) Investigation of the degradation of pitch-based carbon fibers properties upon insufficient or excess thermal treatment. *Sci Rep* 7:4733
 44. Gogotsi Y (2010) High-temperature rubber made from carbon nanotubes. *Science* 330:1332–1333
 45. Nwamba OC, Echeverria E, McIlroy D, Austin A, Shreeve JMS, Aston DE (2019) Thermal modification of graphite for enhanced and sustained electron transport properties. *ACS Appl Nano Mater* 2:228–240
 46. Yan X, Tian L, Murowchick J, Chen X (2016) Partially amorphized MnMoO_4 for highly efficient energy storage and the hydrogen evolution reaction. *J Mater Chem A* 4:3683–3688
 47. Bustos E, Manríquez J, Orozco G, Godínez LA (2005) Preparation, characterization, and electrocatalytic activity of surface anchored, Prussian blue containing starburst PAMAM dendrimers on gold electrodes. *Langmuir* 21:3013–3021
 48. Qiu JD, Peng HZ, Liang RP, Li J, Xia XH (2007) Synthesis, characterization, and immobilization of Prussian blue-modified Au nanoparticles: application to electrocatalytic reduction of H_2O_2 . *Langmuir* 23:2133–2137
 49. Dacarro G, Taglietti A, Pallavicini P (2018) Prussian blue nanoparticles as a versatile photothermal tool. *Molecules* 23:1–20
 50. Agrisuelas J, Bueno PR, Ferreira FF, Gabrielli C, García-Jareño JJ, Gimenez-Romero D, Perrot H, Vicente F (2009) Electronic perspective on the electrochemistry of Prussian blue films. *J Electrochem Soc* 156:P74–P80
 51. Nie P, Shen L, Pang G, Zhu Y, Xu G, Qing Y, Dou H, Zhang X (2015) Flexible metal–organic frameworks as superior cathodes for rechargeable sodium-ion batteries. *J Mater Chem A* 3:16590–16597
 52. Sato O, Einaga Y, Fujishima A, Hashimoto K (1999) photoinduced long-range magnetic ordering of a cobalt–iron cyanide. *Inorg Chem* 38:4405–4412
 53. Liu D, Lv Y, Zhang M, Liu Y, Zhu Y, Zong R, Zhu Y (2014) Defect-related photoluminescence and photocatalytic properties of porous ZnO nanosheets. *J Mater Chem A* 2:15377–15388
 54. Xia L, McCreery RL (1999) Structure and function of ferricyanide in the formation of chromate conversion coatings on aluminum aircraft alloy. *J Electrochem Soc* 146:3696–3701
 55. Smith E, Dent G (2005) Modern Raman spectroscopy—a practical approach. Wiley, Hoboken
 56. Verón MG, Castañeda Trujillo LD, Piro OE, Güida JA (2014) Infrared and Raman spectra of $[\text{Re}(\text{CN})_5\text{NO}]^{3-}$ complex isolated in KCl matrix. *J Mol Struct* 1076:160–164
 57. Suffren Y, Rollet F-G, Reber C (2011) Raman spectroscopy of transition metal complexes: molecular vibrational frequencies, phase transitions, isomers, and electronic structures. *Comments Inorg Chem* 32:246–276
 58. Lee C, Yan H, Brus LE, Heinz TF, Hone J, Ryu S (2010) Anomalous lattice vibrations of single- and few-layer MoS_2 . *ACS Nano* 4:2695–2700
 59. Yan R, Simpson JR, Bertolazzi S, Brivio J, Watson M, Wu X, Kis A, Luo T, Hight Walker AR, Xing HG (2014) Thermal conductivity of monolayer molybdenum disulfide obtained from temperature-dependent Raman spectroscopy. *ACS Nano* 8:986–993

60. Yang D, Sandoval SJ, Divigalpitiya WMR, Irwin JC, Frindt RF (1991) Structure of single-molecular-layer MoS_2 . *Phys Rev B* 43:12053
61. Verble JL, Wieting TJ (1970) Lattice mode degeneracy in MoS_2 and other layer compounds. *Phys Rev Lett* 25:362
62. Mattson EC, Michalak DJ, Veyan JF, Chabal YJ (2017) Cobalt and iron segregation and nitride formation from nitrogen plasma treatment of CoFeB surfaces. *J Chem Phys* 146:052805
63. Nasluskov VA, Kondratenko AV, Neyman KM, Mazalov LN (1986) An SCF XaSW study of the electronic structure and X-ray and photoelectron spectra of Fe(II) and Fe(III) hexacyano complexes in a cluster approach. *Theor Chim Acta* 70:429–441
64. Cataldi TRI, Salvi AM, Centonze D, Sabbatini L (1996) Voltammetric and XPS investigations of polynuclear ruthenium-containing cyanometallate film electrodes. *J Electroanal Chem* 406:91–99
65. Joachim C, Gimzewski JK, Aviram A (2000) Electronics using hybrid-molecular and mono-molecular devices. *Nature* 408:541–548
66. Verkhovtsev AV, Schramm S, Solov'Yov AV (2014) Molecular dynamics study of the stability of a carbon nanotube atop a catalytic nanoparticle. *Eur Phys J D* 68:246
67. Solov'Yov IA, Mathew M, Solov'Yov AV, Greiner W (2008) Liquid surface model for carbon nanotube energetics. *Phys Rev E Stat Nonlinear Soft Matter Phys* 78:051601
68. Norris D, Bawendi M (1996) Measurement and assignment of the size-dependent optical spectrum in CdSe Quantum dots. *Phys Rev B Condens Matter Mater Phys* 53:16338
69. Hubbard J (1963) Electron correlations in narrow energy bands. *Proc R Soc A Math Phys Eng Sci* 276:238–257
70. Essler FHL, Frahm H, Göhmann F, Klümper A, Korepin VE (2005) The one-dimensional hubbard model. Cambridge University Press, Cambridge
71. Samain L, Grandjean F, Long GJ, Martinetto P, Bordet P, Strivay D (2013) Relationship between the synthesis of Prussian blue pigments, their color, physical properties, and their behavior in paint layers. *J Phys Chem C* 117:9693–9712
72. Han L, Tricard S, Fang J, Zhao J, Shen W (2013) Prussian blue @ platinum nanoparticles/graphite felt nanocomposite electrodes: application as hydrogen peroxide sensor. *Biosens Bioelectron* 43:120–124
73. Yang Y, Liu E, Yan X, Ma C, Wen W, Liao X-Z, Ma Z-F (2016) Influence of structural imperfection on electrochemical behavior of Prussian blue cathode materials for sodium ion batteries. *J Electrochem Soc* 163:A2117–A2123
74. Johansson A, Widenkvist E, Lu J, Boman M, Jansson U (2005) Fabrication of high-aspect-ratio Prussian blue nanotubes using a porous alumina template. *Nano Lett* 5:1603–1606
75. Pingarrón JM, Yáñez-Sedeño P, González-Cortés A (2008) Gold nanoparticle-based electrochemical biosensors. *Electrochim Acta* 53:5848–5866
76. Bishop GW, Ahiadu BK, Smith JL, Patterson JD (2017) Use of redox probes for characterization of layer-by-layer gold nanoparticle-modified screen-printed carbon electrodes. *J Electrochem Soc* 164:B23–B28
77. Qian J, Ma D, Xu Z, Li D, Wang J (2018) Electrochromic properties of hydrothermally grown Prussian blue film and device. *Sol Energy Mater Sol Cells* 177:9–14
78. Padigi P, Thiebes J, Swan M, Goncher G, Evans D, Solanki R (2015) Prussian green: a high rate capacity cathode for potassium ion batteries. *Electrochim Acta* 166:32–39
79. Jia S, Zang J, Li W, Tian P, Zhou S, Cai H, Tian X, Wang Y (2018) A novel synthesis of Prussian blue nanocubes/biomass-derived nitrogen-doped porous carbon composite as a high-efficiency oxygen reduction reaction catalyst. *Electrochim Acta* 289:56–64
80. Wessells CD, Peddada SV, Huggins RA, Cui Y (2011) Nickel hexacyanoferrate nanoparticle electrodes for aqueous sodium and potassium ion batteries. *Nano Lett* 11:5421–5425
81. Zhang Y-Z, Cheng T, Wang Y, Lai W-Y, Pang H, Huang W (2016) Flexible supercapacitors: a simple approach to boost capacitance: flexible supercapacitors based on manganese oxides@ MOFs via chemically induced in situ self-transformation. *Adv Mater* 28:5241
82. Agarwal R, Sharma MK, Bhattacharyya K (2016) Prussian blue-manganese hexacyanoferrate nanocomposite as multifunctional high performance electrode material. *ChemistrySelect* 1:3562–3568
83. Yu L, Hu H, Wu HB, Lou XW (2017) complex hollow nanostructures: synthesis and energy-related applications. *Adv Mater* 29:1604563
84. Kolthoff IM, Pearson EA (1931) Stability of potassium ferrocyanide solutions. *Ind Eng Chem Anal Ed* 3:381–382

Publisher's Note Springer Nature remains neutral with regard to jurisdictional claims in published maps and institutional affiliations.